Article

S 2p and P 2p Core Level Spectroscopy of PPT Ambipolar Material and Its Building Block Moieties

E. Bernes, G. Fronzoni, M. Stener, A. Guarnaccio,* T. Zhang, C. Grazioli, F. O. L. Johansson, M. Coreno, M. de Simone, C. Puglia, and D. Toffoli*

Read Online

ACCESS | Metrics & More | Article Recommendations | Supporting Information

ABSTRACT: The near-edge X-ray absorption fine structure (NEXAFS) and X-ray photoelectron (XP) spectra of gas-phase 2,8-bis-(diphenylphosphoryl)dibenzo[*b,d*]thiophene (PPT) and triphenylphosphine oxide (TPPO) have been measured at the S and P $L_{II,III}$-edge regions. The time-dependent density functional theory (TDDFT) based on the relativistic two-component zeroth-order regular approximation approach has been used to provide an assignment of the experimental spectra, giving the contribution of the spin−orbit splitting and of the molecular-field splitting to the sulfur and phosphor binding energies. Computed XP and NEXAFS spectra agree well with the experimental measurements. In going from dibenzothiophene and TPPO to PPT, the nature of the most intense S 2p and P 2p NEXAFS features are preserved; this trend suggests that the electronic and geometric behaviors of the S and P atoms in the two building block moieties are conserved in the more complex system of PPT. This work enables us to shed some light onto the structure of the P−O bond, a still highly debated topic in the chemical literature. Since the S 2p and P 2p NEXAFS intensities provide specific information on the higher-lying localized σ^*(C−S) and σ^*(P−O) virtual MOs, we have concluded that P 3d AOs are not involved in the formation of the P−O bond. Moreover, the results support the mechanism of negative hyperconjugation, by showing that transitions toward σ^*(P−O) states occur at lower energies with respect to those toward π^*(P−O) states.

P2p→σ*(P-O) E_{exc} = 136 eV

P2p→π*(P-O) E_{exc} = 137 eV
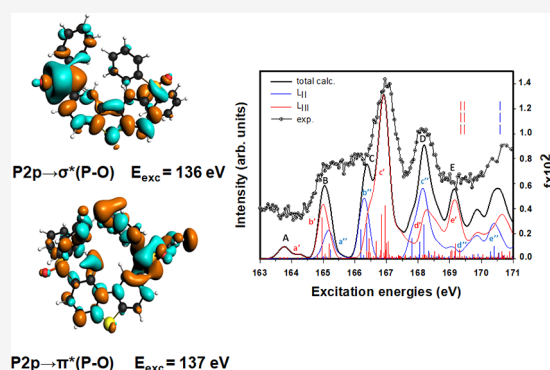
1. INTRODUCTION

During the past decade, numerous advances in the field of organic semiconductor devices have occurred. Currently, a large part of the research is addressing organic light-emitting diodes (OLEDs), and this is due to the synthetic versatility of organic materials, which can be designed with tuned properties, including emission energy, charge transport, and morphological stability.[1,2] In particular, significant efforts have been made on solid-state lighting applications involving phosphorescent OLEDs (PhOLEDs) because of their potential applications in full-color flat-panel displays.[3]

A promising class of host materials in blue PhOLEDs is represented by derivatives of dibenzothiophene (DBT) substituted with diphenylphosphine oxide, such as the 2,8-bis(diphenylphosphoryl)-dibenzo[*b,d*]thiophene (PPT), an ambipolar phosphorescent electron-transporting material, with sky-blue emission, high emission efficiency, and suitable energy levels.[4−6] The PPT chemical structure (Figure 1, panel c) consists of an electron-rich DBT core functionalized by two electron-withdrawing phosphine oxide groups. It has been seen that the device's efficiency is increased when DBT replaces other π-conjugated core analogues such as carbazole and dibenzofuran.[7] In particular, the polycyclic aromatic DBT building block in PPT promotes the hole transport and reduces

the HOMO−LUMO gap, facilitating the electron injection process and introducing a hole-blocking function in the resulting OLED.[7]

Despite these recent developments toward applications, a detailed understanding of the complex electronic processes involved in the mechanisms underlying their potential device applications is still lacking. To fill this gap, advantage can be taken from a detailed knowledge of their electronic structure, as that provided by the use of core−electron spectroscopies such as XPS (X-ray photoelectron spectroscopy) and NEXAFS (near-edge X-ray absorption fine structure). The latter can be used to probe the electronic structure of complex systems, essentially due to the localized nature of the core-hole which is formed upon core excitation.[8]

In this respect, we recently studied the C 1s and O 1s edges of the TPPO and PPT molecules;[9] the present paper aims to complete this study by considering the XP and NEXAFS
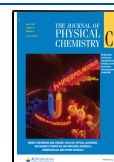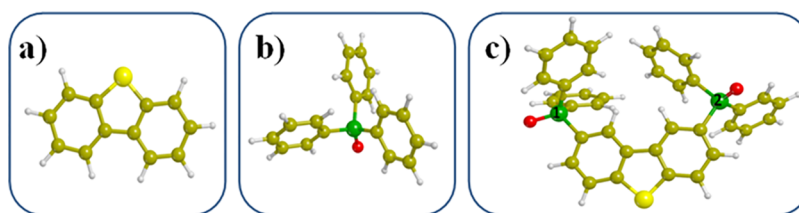
Figure 1. Chemical structures of (a) dibenzothiophene (DBT), (b) triphenylphosphine oxide (TPPO), and (c) 2,8-bis(diphenylphosphoryl)-dibenzo[*b,d*]thiophene (PPT). O atoms in red, S atoms in yellow, and P atoms in green. The two nonequivalent P atoms of PPT are labeled.

spectra of these two systems at the S and P $L_{II,III}$-edges. The comparison with the features of the DBT molecule (see Figure 1, panel a, for the chemical structure) at the S 2p edge[10] will be also considered. To our knowledge, this work represents the first joint experimental and theoretical study of S 2p and P 2p edges on PPT and its DBT and TPPO building blocks. Since the assignment of the NEXAFS P $L_{II,III}$-edge absorption features provides specific information on the involvement of P ns, nd atomic orbitals (AOs) to the virtual molecular states, another outcome of this work is a detailed analysis of the nature of the P−O bond, whose description in terms of atomic orbitals (AOs), contributions of P, O atoms, and the organic residues is still controversial.[11] In our previous study,[9] the O 1s NEXAFS spectra calculations pointed toward a greater participation of O 2p AOs to occupied molecular orbitals (MOs) and supported the mechanism of negative hyperconjugation as well as the stabilization of the π symmetry interaction in the P−O bond with respect to the σ one in the occupied MOs. We expect that the present results on the P $L_{II,III}$-edge can support these findings.

Both the coupling between different excitation channels arising from the 2p degenerate core-holes and relativistic spin−orbit (SO) coupling effects need to be included in the computational protocol used to simulate the NEXAFS spectra at the $L_{II,III}$-edge region, to obtain a quantitative description of the series of transitions converging to the L_{II} and L_{III}-edges. In this paper we used TDDFT and the relativistic two-component zeroth-order regular approximation approach (ZORA), as implemented in the ADF (Amsterdam density functional) code for the treatment of core electron excitations. Core ionization energies (IEs), measured by XPS, are also useful for material characterization due to their sensitivity to the local chemical and physical environment of the ionized atomic site. In the ZORA-TDDFT scheme, the absolute IP's values are identified as minus the ground-state Kohn−Sham spinors eigenvalues, while the intensity of the primary lines has been set arbitrary to unity multiplied by the number of symmetry equivalent sites (for the two P atoms in PPT). This representation stems from the difficulty to calculate the μ_{ft} dipole transition moment between the core orbital and the continuum orbital of the unbound photoelectron, when conventional basis sets, like Gaussian or Slater functions, are used, and is supported by the sufficiently high photon energy employed in the S 2p and P 2p XP experiments (see the Experimental Section) with respect to the S 2p and P 2p binding energies (BEs).

The plan of this paper is the following: Sections 2 and 3 describe the experimental setup and the computational method employed, respectively. A discussion of the results is presented in Section 4, where the assignment of S 2p and P 2p XP and NEXAFS spectra of TPPO and PPT is carried out, while

conclusions and perspectives are summarized in the final Section 5.

2. EXPERIMENTAL SECTION

The investigated molecules were purchased from Sigma-Aldrich (TPPO, with purity 98%) and from Lumtec (PPT, with purity >99%). At room temperature both TPPO and PPT are crystalline solids, and the gas phase was reached by sublimation in vacuum employing a in-house built resistive furnace. The sublimation temperatures were 128 °C for TPPO and 251 °C for PPT. Both temperatures were reached after a gradient purification treatment of at least 20 h.

The experiments were carried out at the Gas Phase beamline of the Elettra-Sincrotrone Trieste[12] by using an end-station equipped with a Scienta SES-200 electron analyzer.[13] The angle between the detection direction and the electric vector of the linearly polarized light was 54° (magic angle configuration). Photoemission spectra of the S 2p core levels were collected using a photon energy of 260 eV and an energy resolution of about 111 meV; S 2p spectra of SF_6 were also collected for energy calibration (180.21 eV for $2p_{3/2}$ and 181.5 eV for $2p_{1/2}$).[14,15] P 2p spectra were collected at a photon energy of 220 eV with an energy resolution of about 114 meV; the energy calibration was performed by measuring in the same experimental window both S 2p and P 2p doublets and calibrating with respect to the previously calibrated S 2p XPS doublet of the corresponding molecule.

NEXAFS spectra at the S, P $L_{II,III}$-edges were acquired in the total ion yield (TIY) mode with an electron multiplier and normalized with respect to the photon flux by using a calibrated Si photodiode (AxVU100 IRD). In the case of S, the calibration of the photon energy was performed with respect to the characteristic $T_{1u} (a_{1g})$-3/2 $T_{1u} (a_{1g})$-1/2 transition of SF_6 (respectively at 172.5 and 173.6 eV[16]) collected simultaneously. The photon energy resolution was 80 meV. The P $L_{II,III}$-edge was calibrated by taking simultaneous spectra of the samples and of Xe, whose characteristic Xe 4p transition (141.8 eV) is well-known.[17] The peak resolution of the P $L_{II,III}$-edge spectra was equal to 50 meV for both TPPO and PPT.

The experimental XPS data were analyzed by means of the XPST (X-ray photoelectron spectroscopy tools) package for IGOR PRO by Dr. Martin Schmid. The molecular-field splitting was extracted from the S 2p and P 2p spectra by applying an empirical model similar to the one by Giertz et al.[18] In the first step, the data were fitted using one single asymmetric Voigt function for S $2p_{1/2}$ and P $2p_{1/2}$ peaks. The same asymmetric Voigt function was then superimposed twice on the S $2p_{3/2}$ and P $2p_{3/2}$ peaks. Then appropriate shifts have been applied to the calculated eigenvalues in order to better align them with the corresponding experimental fitted curves.

3. COMPUTATIONAL DETAILS

The geometry optimization of TPPO and PPT has been carried out at the density functional theory (DFT[19]) level, within the local-density approximation (LDA) by using the Vosko, Wilk, Nusair (VWN) exchange and correlation (xc) functional[20] and the triple ζ polarized (TZP) basis set of Slater type orbitals (STOs) from the ADF (Amsterdam density functional) database.[21,22] No symmetry constraints were imposed during the optimization. Indeed, as revealed by crystallographic studies, TPPO has no symmetry because the rotations of the phenyl rings about the P−C bonds are not identical.[23,24] Moreover, the O−P−C angles are greater than the tetrahedral angle due to the partial multiple bond character of the P−O bond, while the C−P−C angles are smaller than it.[24] Analogous considerations can be made in the case of PPT, where the lack of symmetry is a consequence of steric avoidance between the two diphenylphospine oxide moieties. Two different conformations have been taken into account for TPPO, one derived from X-ray diffraction data[25] and one predicted in vacuo at the MP2/cc-pVTZ level.[26] Since we found out that the C 1s NEXAFS spectra of the two conformers are quantitatively very similar,[9] we chose to perform the computation and the assignment of the P 2p NEXAFS spectrum of TPPO only on the structure derived from the XRD data to which also all results of our previous study refer. The optimized Cartesian coordinates of DBT, TPPO, and PPT are reported in the Supporting Information.

The S 2p and P 2p NEXAFS spectra calculations have been performed within TDDFT by using the two-component ZORA approximation[27] implemented in the ADF code[21,22,28] within the adiabatic local density approximation (ALDA) to the exchange-correlation (xc) kernel. Here, we will only recall the main steps of the TDDFT formalism when dealing with core electron excitations, referring the reader to the literature[29,30] for a more detailed account of the method.

Within linear response TDDFT,[31] the excitation spectrum is obtained through the solution of the following eigenvalue equation by means of Davidson's iterative algorithm:[32]

$$\Omega F_I = \omega_I^2 F_I \tag{1}$$

The elements of the Ω matrix are given by

$$\Omega_{ia\sigma,bj\tau} = \delta_{\sigma\tau}\delta_{ij}\delta_{ab}(\epsilon_a - \epsilon_i)^2 + 2\sqrt{(\epsilon_a - \epsilon_i)}\frac{\partial F_{ia}}{\partial P_{jb}}\sqrt{(\epsilon_b - \epsilon_j)} \tag{2}$$

where indices i and j denote occupied spinors in the KS ground state, while indices a and b denote virtual spinors and ε_i and ε_a are the corresponding KS energies. The Fock and the density matrix are denoted by $\mathbf{F}$ and $\mathbf{P}$ while $\frac{\partial F_{ia}}{\partial P_{jb}}$ are the elements of the coupling matrix. Squared excitation energies ω_I^2 are then obtained as the eigenvalues of eq 1, while oscillator strengths can be extracted from the eigenvectors F_I. However, due to its limitation to the extraction of a relatively small number of lowest eigenvalues and eigenvectors, Davidson's algorithm is not able to efficiently solve eq 1, as core excitation energies lie very high in the excitation spectrum. This limitation can be overcome by invoking the core−valence separation approximation (CVS) introduced by Cederbaum et al.;[33,34] the 1h-1p space spanned by the solutions of eq 1 can be reduced by including only the most important configurations.[35] Therefore, within this approximation, indices i and j run only over the core−shell under study (in the case of 2p excitations, over the two subshells, namely $2p_{1/2}$ and $2p_{3/2}$, allowing a mixing of only those initial states). As a consequence, eq 1 is solved in a smaller 1h-1p subspace, and the core excitations now correspond to its lowest roots, hence allowing an effective use of Davidson's algorithm. This approximation neglects the coupling between core excitations and valence excitations to the continuum, and the treatment of the continuum states does not need to be included in the computational scheme. In addition, one can expect that the coupling between core excitations and valence ionizations is very small.[35]

For the nonexcited atoms, an all-electron DZP basis set, optimized for ZORA calculations[36] and available from the ADF database, has been used. For both P and S excited atoms, two shells of s, p, d, and f diffuse functions with exponents obtained with the even-tempered criterion ($\beta = 1.7$) have been added to the QZ4P ZORA basis set to obtain a [13s, 9p, 5d, 6f] basis, referred to as ET-QZ4P-2DIFFUSE. We include diffuse functions in the basis set to describe transitions to diffuse orbitals (Rydberg excited states) close to the ionization threshold. Two different xc functionals have been tested in the self-consistent field (SCF) calculations: the LB94 xc potential[37] with the ground-state electron configuration and the hybrid B3LYP.[38−40] Since the former gives a slightly better agreement with the experimental data for both XP and NEXAFS spectra, in the following section, we will discuss the LB94 results and provide the B3LYP outcomes in the Supporting Information. Furthermore, the assignment of the experimental features of the NEXAFS spectra to 1h-1p core-excited states is not significantly affected by the actual choice of the xc potential. A note on the computational efficiency of the CVS-TDDFT method when applied to large molecular systems, such as PPT, is in order. In such cases, the density of the manifold of core-excited states is such that the number of roots of eq 1 that need to be extracted to cover the excitation energy range up to the P $L_{II,III}$ ionization threshold is very high (>1000) so that even within the CVS approximation the Davidson's iterative algorithm could become numerically unstable. In this work, the computed P 2p TDDFT NEXAFS profiles are therefore limited to the energy interval determined by the largest roots that can be safely computed iteratively (700 and 1000 for TPPO and PPT, respectively). This is not a problem when employing the LB94 potential but, due to the specific implementation within ADF, poses several limitations when using hybrid functionals such as B3LYP.

For both xc functionals, the calculated S 2p and P 2p NEXAFS spectra have been deconvoluted into the two manifolds of excited states converging to the L_{III} and L_{II}-edges. This has been done by multiplying the oscillator strength of each transition by the coefficient squared of the configurations describing excitations from the $2p_{3/2}$ and $2p_{1/2}$ levels. In the calculation of the P 2p NEXAFS spectra, we included the coupling among the excitation channels of both P centers, since preliminary calculations revealed that their coupling is mandatory for achieving a quantitative reproduction of the experimental NEXAFS intensity distribution. Core excitation energies are computed from scaled ZORA spinor eigenvalues.

The raw NEXAFS spectra have been convoluted with Gaussian functions of constant full width at half-maximum (fwhm) values (equal to 0.3 and 0.5 eV for S 2p and P 2p NEXAFS spectra, respectively). The use of Gaussian functions to smooth calculated discrete lines allows for a pragmatic

inclusion of an average lifetime of the core-excited states, beside facilitating the comparison with the experimental data. Although vibrational effects can also affect the line-shape and broadening of the core-ionized and -excited spectra, they have not been considered in the present work.

Theoretical ionization threshold values are identified as minus the DFT eigenvalues obtained within the ZORA approximation and the LB94 xc functional

$$IP = -\varepsilon_{2p} \qquad (3)$$

where ε_{2p} represents the eigenvalue of the $2p_{1/2,3/2}$ spin orbitals. These IP values are also employed to simulate the S 2p and P 2p XP spectra; when comparing with the experimental measurements, the theoretical IPs have been shifted to lower BEs by 1.23 eV (S 2p PPT), 0.90 eV (P 2p TPPO), and 1.02 eV (P 2p PPT). The energy scale of the calculated NEXAFS spectra has been shifted to align the energy position of the maxima of the first absorption band. Applied shifts were equal to +0.3, +2.25, and +2.20 eV for the S $L_{II,III}$-edge excitations in PPT and P $L_{II,III}$-edge excitations in TPPO and PPT, respectively.

4. RESULTS AND DISCUSSION

In the following two subsections we will analyze our calculations to assign the experimental XP and NEXAFS
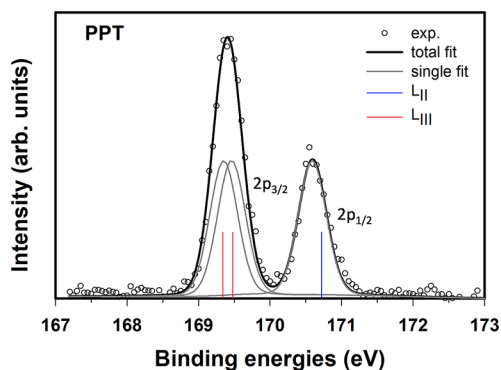
Figure 2. S 2p XP spectrum of PPT. Circles: experimental data; black line: total fit obtained according to the procedure described in the text. Vertical colored bars: LB94 IPs shifted by −1.23 eV for a better matching with the experimental curve. The light gray curves are the L_{II} (centered around the blue vertical bar) and L_{III} (centered around the red vertical bars) S 2p components obtained by the fitting procedure using a single and two asymmetric Voigt functions, respectively.

Table 1. Theoretical LB94 S 2p IPs and Experimental BEs of PPT[a]

| | PPT | |
edge	theory[b]	single fit
L_{II}	170.72	170.59
L_{III}	169.48	169.46
L_{III}	169.34	169.35

[a]All values are expressed in eV. [b]Calculated IPs shifted by −1.23 eV.

spectra of TPPO and PPT. We will focus on the XP spectra in the first subsection, while NEXAFS spectra will be considered in the final subsection.

The intensity distribution of the $L_{II,III}$-edge spectra is governed by the interplay of two main effects: the relativistic
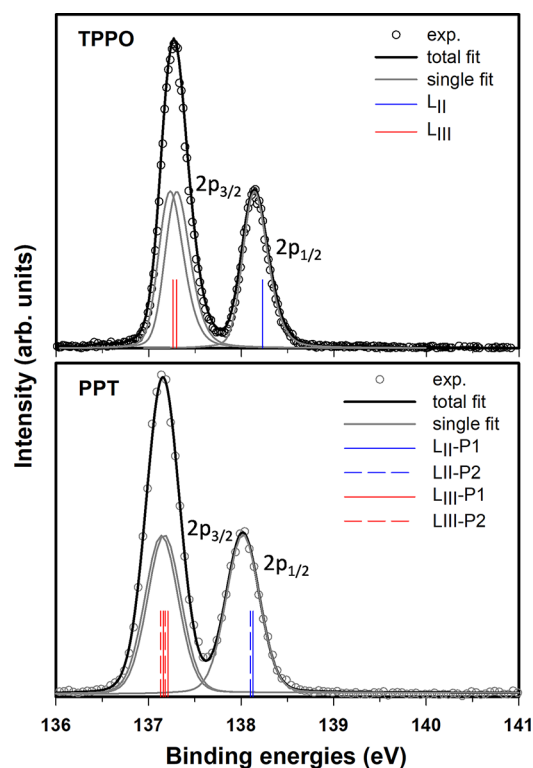
Figure 3. P 2p XP spectra of TPPO (upper panel) and PPT (lower panel). Circles: experimental data; black line: total fit obtained according to the procedure described in the text. Vertical colored bars: LB94 IPs shifted by −0.90 and −1.02 eV for TPPO and PPT, respectively, for a better matching with the experimental curves. The light gray curves are the L_{II} (centered around the blue vertical bar) and L_{III} (centered around the red vertical bars) S 2p components obtained by the fitting procedure using a single and two asymmetric Voigt functions, respectively.

Table 2. Theoretical LB94 P 2p IPs and Experimental BEs of TPPO and PPT[a]

			PPT		
	TPPO		theory[c]		
edge	theory[b]	single fit	P1	P2	single fit
L_{II}	138.23	138.14	138.13	138.10	138.01
L_{III}	137.30	137.30	137.21	137.18	137.17
L_{III}	137.26	137.23	137.16	137.13	137.14

[a]All values are in eV. [b]Calculated IPs shifted by −0.90 eV. [c]Calculated IPs shifted by −1.02 eV.

SO interaction and the *molecular-field splitting*. SO coupling lowers the degeneracy of the 2p core hole by splitting the 2p core orbital energies into the two SO components $2p_{3/2}(L_{III})$ and $2p_{1/2}$ (L_{II}). The molecular-field splitting further lowers the degeneracy of the $2p_{3/2}$ state and produces a splitting into two components, as a consequence of the anisotropic molecular potential. Moreover, configuration mixing plays an important role in determining the correct intensity distribution among the 2p transitions. All these effects are included in the computational method employed.

4.1. Assignment of the Experimental S 2p and P 2p XP Spectra. S 2p XP spectra of PPT are shown in Figure 2, together with the results of the fitting procedure detailed in Section 2, while a comparison with the S 2p results for DBT[10] has been included in the Supporting Information (Figure S1).

Table 3. Peak Assignments of the S L_{II,III}-Edge NEXAFS Spectrum of PPT[a]

peak/subpeak	calcd E-shifted[b] (eV)	$f \times 10^2$	EDGE	assignment	exptl E (eV)
A/a′	163.62	1.39×10^{-2}	L_{III}	155 A (LUMO+2)/ π^*(C=C)	-
	163.65	1.25×10^{-2}		156 A/π^*(C=C)	
	163.76	1.41×10^{-2}		155 A	
	163.77	1.13×10^{-2}		157 A/π^*(C=C)	
	163.85	2.90×10^{-3}		158 A/π^*(C=C)	
	163.87	1.41×10^{-2}		157 A	
	163.99	4.05×10^{-3}		158 A	
	164.20	1.06×10^{-2}		163 A/π^*(C=C)	
	164.32	1.08×10^{-2}			
B/a″	164.99	1.92×10^{-2}	L_{II}	155 A	165.30
	165.02	6.41×10^{-3}		156 A	
	165.10	2.33×10^{-2}		157 A	
	165.22	3.64×10^{-3}		158 A	
	165.23	8.98×10^{-2}			
	165.56	1.21×10^{-2}		163 A	
B/b′	164.82	3.58×10^{-2}	L_{III}	164 A/σ^*(C−S)- Rydberg mixed	
	164.97	0.34			
	165.06	4.39×10^{-2}		165 A/σ^*(C−S)- Rydberg mixed	
	165.19	0.22		164 A	
C/b″	166.20	0.24	L_{II}	164 A	-
	166.27	3.03×10^{-2}			
	166.29	3.27×10^{-2}		165 A	
	166.37	0.36			
C/c′	166.44	5.80×10^{-2}	L_{III}	168 A/σ^*(P−O)- Rydberg mixed	166.75
	166.45	0.18			
	166.48	5.17×10^{-2}		167 A/σ^*(C−H)- Rydberg mixed	
	166.68	0.14		171 A/σ^*(C−H)- Rydberg mixed	
	166.80	6.78×10^{-2}		170 A/σ^*(P−O)- Rydberg mixed	
	166.84	0.36		172 A/Rydberg	
	166.85	0.13		171 A	
	166.92	4.99×10^{-2}		172 A	
	166.94	1.66×10^{-2}		173 A/σ^*(C−H)- Rydberg mixed	
	166.97	0.43		172 A	
	166.99	0.14		172 A	
	167.06	0.14		174 A/σ^*(C−H)- Rydberg mixed	
	167.19	2.18×10^{-2}			
	167.20	0.18			
D/c″	167.81	0.17	L_{II}	168 A	168.00
	168.04	0.14		171 A	
	168.18	0.31		172 A	
	168.19	6.76×10^{-2}			
	168.32	6.93×10^{-2}		173 A	
	168.43	3.28×10^{-2}		174 A	
	168.44	1.35×10^{-2}			
D/d′	168.35	5.88×10^{-2}	L_{III}	189 A/Rydberg	
	168.52	6.31×10^{-2}		191 A/σ^*(C−H)- Rydberg mixed	
E/e′	169.03	6.39×10^{-2}	L_{III}	196 A/σ^*(C−H)- Rydberg mixed	-
	169.06	8.45×10^{-2}		197 A/σ^*(C−H)- Rydberg mixed	
	169.16	6.63×10^{-2}		198 A/σ^*(C−H)- Rydberg mixed	
	169.18	0.12		200 A/σ^*(C−H)- Rydberg mixed	
	169.32	7.27×10^{-2}			

[a]Only the main transitions, computed at the TDDFT LB94 level, are reported. [b]Calculated excitation energies shifted by +0.3 eV to match the energy position of the first experimental peak.
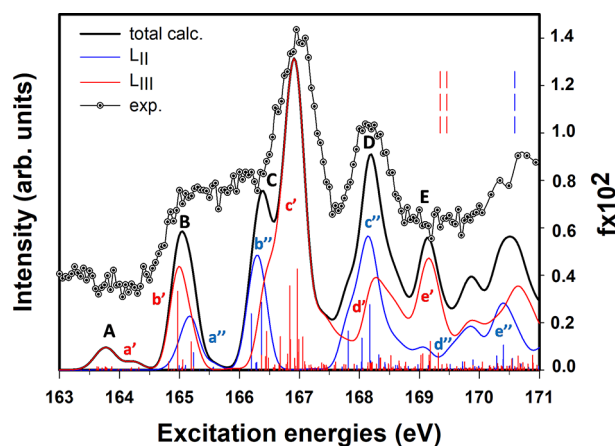
Figure 4. S L_{II,III}-edge NEXAFS spectrum of PPT. Circles: experimental data; black solid line: LB94 TDDFT results. Deconvolution of the calculated S 2p spectrum into excitations converging to the L_{III} (red solid line and vertical red bars) and L_{II} (blue solid line and vertical blue bars) edges is also shown. The energy scale of the theoretical data has been shifted by +0.3 eV to match the position of the first experimental peak. Blue and red vertical bars denote the experimental L_{II,III}-edges. The left vertical axis refers to the experimental intensities (plotted in arbitrary units), while the right vertical axis refers to computed oscillator strengths (multiplied by a factor of 100).

The experimentally fitted BEs together with the LB94 IPs of PPT are also listed in Table 1.

We assign the more intense lower-energy photoelectron peak of Figure 2 to the $^2P_{3/2}$ states, while the peak at 170.6 eV is assigned to the $^2P_{1/2}$ state. The fitting reproduces very well the experimental data and permits the extraction of the molecular-field splitting of the S $2p_{3/2}$ component. The experimental trend is qualitatively reproduced by theory, although the KS eigenvalues overestimate the fitted BEs by about 1.23 eV; this can be ascribed to the too attractive character of the LB94 xc potential. Within standard TDDFT, the 1h-1p excitation space is built from the KS ground-state orbitals (which are therefore not relaxed), and the IPs of the 2p electrons, according to Koopmans' theorem, are identified as minus the KS energies of the relative spinors. The discrepancy with the observed trend could be in principle recovered by ΔKS calculation of IPs[28] as well as by the use of relaxed orbitals.[29] On the other hand, the SO splitting ($\Delta_{3/2,1/2}$) value, computed as the difference between the energy of the $^2P_{1/2}$ state and the average energy of the $^2P_{3/2}$ states, is in very good agreement with the experimental value, being the discrepancy of the two sets of data of 120 meV (1.31 eV computed, 1.19 eV experimental), and confirms a posteriori the accuracy of the computational method employed. The computed molecular-field splitting, equal to 140 meV, is in good agreement with the experimental value derived from the fit (equal to 110 meV).
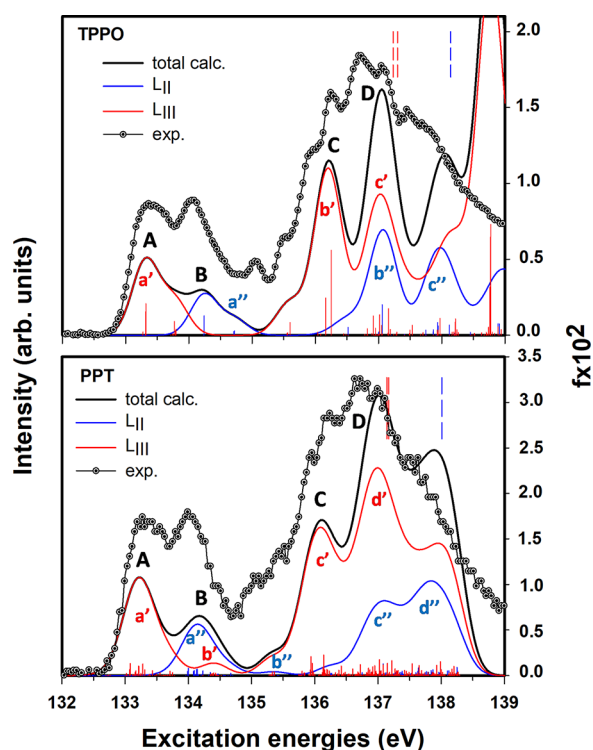
Figure 5. P $L_{II,III}$-edge NEXAFS spectra of TPPO (upper panel) and PPT (lower panel). Circles: experimental data; black solid line: LB94 TDDFT results. Deconvolution of the calculated spectra into excitations converging to the L_{III} (red solid line and vertical red bars) and L_{II} (blue solid line and vertical blue bars) edges is also shown. The energy scale of the theoretical data has been shifted by +2.25 and +2.20 eV, respectively, for TPPO and PPT to match the position of the first experimental peak. The experimental $L_{II,III}$-edges are also shown (blue and red vertical dashed bars) within each spectrum. The left vertical axis refers to the experimental intensities (plotted in arbitrary units), while the right vertical axis refers to computed oscillator strengths (multiplied by a factor of 100).

Table 4. Peak Assignments of the P $L_{II,III}$-Edge NEXAFS Spectrum of TPPO[a]

peak/ subpeak	calcd				exptl
	E-shifted[b] (eV)	$f \times 10^2$	EDGE	assignment	E (eV)
A/a′	133.32	0.21	L_{III}	74 A (LUMO)/ π^*(C=C)	133.16
	133.77	9.19×10^{-2}		79 A/π^*(C=C)	
	133.79	4.14×10^{-2}			
B/a″	134.24	0.13	L_{II}	75 A/π^*(C=C)	134.08
	134.71	2.41×10^{-2}		77 A/π^*(C=C)	
	134.72	2.96×10^{-2}		79 A	
C/b′	135.60	8.44×10^{-2}	L_{III}	80 A/σ^*(C−H)- Rydberg mixed	135.48
	136.16	0.25		83 A/σ^*(P−O)- Rydberg mixed	135.88
	136.25	0.58			136.20
D/b″	136.52	5.12×10^{-2}	L_{II}	80 A	136.68
	137.06	0.21		83 A	137.08
D/c′	136.82	4.33×10^{-2}	L_{III}	85 A/σ^*(C−H)- Rydberg mixed	137.48
	136.92	0.13		87 A/σ^*(C−H)- Rydberg mixed	
	136.95	4.92×10^{-2}			
	137.02	0.17		88 A/σ^*(C−H)- Rydberg mixed	
	137.05	9.25×10^{-2}		89 A/π^*(P−O)- Rydberg mixed	
	137.16	0.33		90 A/π^*(P−O)- Rydberg mixed	
	137.18	5.46×10^{-2}			
	137.20	0.17			

[a]Only the main transitions, computed at the TDDFT LB94 level, are reported. [b]Calculated excitation energies shifted by +2.25 eV to match the energy position of the first experimental peak.

From a comparison of the S 2p spectrum of PPT with that of DBT (see Figure S1), one sees that the two spectra are very similar, as well as their SO splitting. A small BE increase (of about 0.1 eV) of the photoelectron peaks is found in going from DBT to PPT (compare Table S1 and Table 1): this reflects a small local change of the electron density around sulfur (lower shielding effect), as a consequence of the addition of two electron-withdrawing phosphine oxide moieties in PPT. The value of the molecular-field splitting predicted by theory is similar for DBT and PPT; this is in line with the comparable geometrical environment of the S atom in the two molecules.

Figure 3 displays the X-ray photoelectron spectra of the P 2p core levels of TPPO and PPT, together with the results of the fit of the experimental line-shapes as described in Section 2. Theoretical LB94 IPs are also reported in the figure, while B3LYP IPs are reported in Table S2 of the Supporting Information.

The experimental BEs are reported in Table 2 along with the computed LB94 P 2p IPs (see Figure 1, panel c, for the labeling of the two nonequivalent P atoms).

An analysis of Figure 3 reveals that the shape of the photoelectron spectra of the two molecules is very similar; indeed, a stronger photoelectron peak, assigned to the $^2P_{3/2}$ states, is observed at lower BEs, while the band at higher energy is assigned to the $^2P_{1/2}$ state. Their energy separation

corresponds to the SO splitting of the 2p SO components. A small decrease (of about 100 meV) of the L_{III} and L_{II} experimental BEs is found in going from TPPO to PPT (see Table 2), as a result of the replacement of a single phenyl ring of TPPO with one condensed ring of the DBT moiety in PPT. The experimental data are well reproduced by the fits, which permit the obtaining of an experimental estimate of the molecular-field splitting of the P $2p_{3/2}$ states. Moreover, the fact that the two diphenylphospine oxide moieties point out toward different directions due to steric hindrance causes a splitting of the P $2p_{3/2}$ signal into two very narrowly spaced components, separated by 30 meV. Furthermore, Table 2 reveals that the shielding effect on the BEs is lower than the molecular-field splitting. We can conclude that the energy separation of the two doublets of the lower-energy band of the PPT XP spectrum is mainly determined by the anisotropic molecular potential which splits the P $2p_{3/2}$ states by about 50 meV.

As concerns the comparison between experiment and theory, the discrepancy between the theoretical IPs and the fitted BEs is about 0.9 eV for TPPO and about 1 eV for PPT; the reason for these discrepancies in the absolute values is again due to the too attractive character of the LB94 xc potential, and considerations analogous to those made when discussing the S 2p XP spectra can be made here. However, the computed SO splitting among the L_{III} and L_{II} P 2p thresholds is in good agreement with the experimental value. Indeed, the computed SO splitting is equal to 950 meV for both molecules, in line with the experimental value of about 870 meV; this still confirms that relativistic effects are rather well accounted for by the ZORA formalism. The calculated molecular-field splitting

Table 5. Peak Assignments of the P L$_{II,III}$-Edge NEXAFS Spectrum of PPT[a]

peak/subpeak	core-hole site	E-shifted[b] (eV)	$f \times 10^2$	EDGE	assignment	E (eV)
A/a′	P2	133.07	6.40×10^{-2}	L$_{III}$	154 A (LUMO+1)/π^*(C=C)	133.39
	P2	133.08	0.13			
	P1	133.16	3.61×10^{-2}		155 A/π^*(C=C)	
	P1	133.17	5.03×10^{-2}		156 A/π^*(C=C)	
	P1	133.21	0.10			
	P1	133.22	9.98×10^{-2}			
	P2	133.28	0.13		157 A/π^*(C=C)	
	P2	133.31	6.29×10^{-2}			
	P2	133.43	5.27×10^{-2}		158 A/π^*(C=C)	
	P1	133.71	4.76×10^{-2}		163 A/π^*(C=C)	
	P1	133.75	3.09×10^{-2}			
B/a″	P2	133.99	4.63×10^{-2}	L$_{II}$	154 A	133.99
	P2	134.00	8.06×10^{-2}			
	P1	134.08	4.29×10^{-2}		155 A	
	P1	134.09	5.42×10^{-2}			
	P1	134.13	6.77×10^{-2}		156 A	
	P1	134.14	6.85×10^{-2}			
	P2	134.23	4.98×10^{-2}		157 A	
	P2	134.35	3.35×10^{-2}		158 A	
B/b′	P2	134.38	2.19×10^{-2}	L$_{III}$	164 A/π^*(C=C)	
	P1	134.40	2.64×10^{-2}			
	P2	134.43	2.54×10^{-2}			
C/b″	P1	135.32	9.39×10^{-3}	L$_{II}$	164 A	135.23
	P2	135.35	9.23×10^{-3}			
	P1	135.41	3.90×10^{-3}		165 A/Rydberg	
C/c′	P1	135.33	4.24×10^{-2}	L$_{III}$	166 A/Rydberg	135.91
	P2	135.36	4.01×10^{-2}			136.24
	P1	135.80	4.61×10^{-2}		167 A/Rydberg	
	P2	135.93	6.18×10^{-2}		168 A/σ^*(P−O)-Rydberg mixed	
	P1	135.94	0.21			
	P1	135.96	0.14			
	P1	135.97	5.02×10^{-2}		169 A/σ^*(C−H)-Rydberg mixed	
	P1	136.13	9.16×10^{-2}		170 A/σ^*(P−O)-Rydberg mixed	
	P1	136.14	0.23			
	P1	136.15	7.05×10^{-2}		171 A/σ^*(C−H)-Rydberg mixed	
	P2	136.19	6.80×10^{-2}			
	P1	136.20	6.15×10^{-2}			
	P2	136.23	5.00×10^{-2}			
	P1	136.38	5.86×10^{-2}		173 A/σ^*(C−H)-Rydberg mixed	
	P2	136.42	0.11			
	P1	136.48	3.67×10^{-2}		174 A/Rydberg	
D/c″	P2	136.75	3.18×10^{-2}	L$_{II}$	167 A	136.72
	P2	136.89	6.20×10^{-2}		168 A	
	P1	137.04	5.18×10^{-2}		170 A	
	P1	137.08	0.16			
	P1	137.12	3.14×10^{-2}		171 A	
D/d′	P2	136.60	7.24×10^{-2}	L$_{III}$	175 A/σ^*(C−H)-Rydberg mixed	136.99
	P1	136.68	3.94×10^{-2}		176 A/Rydberg	
	P2	136.72	0.12		177 A/σ^*(C−H)-Rydberg mixed	
	P2	136.82	3.29×10^{-2}		178 A/Rydberg	
	P2	136.84	4.31×10^{-2}			
	P1	136.85	9.86×10^{-2}		179 A/σ^*(C−H)-Rydberg mixed	
	P1	136.87	8.15×10^{-2}		180 A/σ^*(C−H)-Rydberg mixed	
	P1	136.90	5.98×10^{-2}		181 A/σ^*(C−H)-Rydberg mixed	
	P1	136.91	5.58×10^{-2}			
	P1	136.92	6.02×10^{-2}			
	P1	136.95	0.11			
	P1	136.97	4.95×10^{-2}		182 A/σ^*(P−O)-Rydberg mixed	
	P1	137.02	0.20			

Table 5. continued

| peak/subpeak | calcd | | | EDGE | assignment | exptl |
	core-hole site	E-shifted[b] (eV)	$f \times 10^2$			E (eV)
	P1	137.05	5.44×10^{-2}		183 A/σ*(P−O)-Rydberg mixed	
	P2	137.10	3.35×10^{-2}			

[a]Only the main transitions, computed at the TDDFT LB94 level, are reported. [b]Calculated excitation energies shifted by +2.2 eV to match the energy position of the first experimental peak.

is equal to 40 meV for TPPO (see Table 2), in good agreement with the measured value of 70 meV. A slightly higher value is found for PPT (50 meV compared with 30 meV derived from the experimental measurements).

4.2. Assignment of the Experimental S and P L-Edge NEXAFS Spectra. We start this discussion by assigning the measured absorption bands of the PPT S 2p NEXAFS spectrum to the dominant 1h-1p core excited configurations as obtained from the ZORA TDDFT LB94 calculations. The results are collected in Table 3 and displayed in Figure 4, where the experimental data are compared with the calculated profile. We report in the Supporting Information (Figure S2, upper panel) the NEXAFS spectrum of the DBT core of PPT taken from our recent work[10] in order to investigate the evolution of the spectrum in going from the DBT building block to PPT. The S 2p NEXAFS spectrum of PPT calculated by using the B3LYP xc potential is included in Figure S3 of the Supporting Information. Plots of selected virtual KS MOs are displayed in Figure S5. The complication inherent in the assignment of the S 2p core excitation spectrum is the presence of two series of transitions from the 2p SO core-hole components converging to the L_{III} and L_{II} thresholds, which overlap due to the small L_{III}-L_{II} SO splitting (which is around 1.2 eV). Further complexity is introduced by the redistribution of the intensity among the final excited states derived from the configuration mixing included in the TDDFT scheme. To facilitate the assignment, we applied a deconvolution of the computed spectra into the two series of transitions corresponding to the two SO components of the 2p hole states, as described in Section 3. In the discussion, we will refer to Table 3 where each band of the spectrum is associated with the character of the final MO involved in the dominant 1h-1p excitations contributing to each final excited state.

The total calculated S 2p NEXAFS spectrum of PPT is characterized by a low-lying weak spectral feature (peak A) which arises from several S $2p_{3/2}$ transitions toward final MOs with a strong π*(C=C) valence antibonding character. These transitions have low intensity, consistently with the very small S ns, nd AO weights of the involved final MOs as well as with their high intensity observed in the C K-edge NEXAFS spectrum.[9] The corresponding transitions starting from the S $2p_{1/2}$ level are centered at 165 eV (subpeak a″, in blue) and contribute to the higher-energy portion of band B. The energy separation of a′ and a″ subpeaks is 1.2 eV, the latter being close to both the calculated (1.31 eV) and the experimental (1.19 eV) values of the L_{III}/L_{II} SO splitting, thus confirming our assignment. The main component of peak B (subpeak b′) arises from the L_{III} transitions toward final MOs with σ*(C−S) valence antibonding character with significant S diffuse s and d atomic components. Subpeak b″ contributes to the lower-energy side of the broad and strong band C which dominates the NEXAFS spectrum. Again, we observe a close match between the energy separation of the b′ and b″ subpeaks (about 1.3 eV) and the experimental SO splitting. Subpeak c′,

which is contributed by a manifold of transitions originating from the S $2p_{3/2}$ levels, carries a large portion of the intensity of band C. The most intense transitions involve virtual MOs with mixed valence/Rydberg or pure Rydberg character with significant S ns, nd AO contributions. The valence character of these transitions involves both σ*(C−H) and σ*(P−O) MOs. The SO partner feature of subpeak c′ (subpeak c″) contributes to the lower-energy side of peak D, while the higher-energy side (subpeak d′) is associated with $2p_{3/2}$ excitations toward virtual states of mixed valence/Rydberg character. Excitations of this nature also extend in the energy region of peak E, just below the L_{III} ionization thresholds. Since the SO partners of subpeaks d′ and e′ (subpeaks d″ and e″, respectively) are found just above the L_{III} ionization thresholds, they have been not included in Table 3. The good agreement between the TDDFT spectrum and the experimental one allows us to be confident of the proposed assignment.

Some strict similarities between the NEXAFS spectra of PPT and its DBT core emerge from a comparison of the upper and lower panels of Figure S2 (reported in the Supporting Information). In particular, the position of band B is relatively well-conserved in going from DBT to PPT, as well as the valence character, σ*(C−S), of the virtual states. Moreover, both spectra are dominated by peak C, visible at around 166−167 eV, for which a similar assignment can be proposed, specifically to L_{II} transitions to virtual σ*(C−S) states and L_{III} transitions to virtual MOs of mixed valence-Rydberg character. In PPT, this peak is however also contributed by transitions to σ*(P−O) virtual states. At higher energy, a strict correspondence of the spectral nature and shape is hampered by the increasing number of overlapping transitions to diffuse MOs. To conclude this discussion, the fact that the most distinctive features of the NEXAFS spectra of DBT and PPT have a similar nature (energy position of the bands and their assignment) is a direct consequence of the localized nature of both initial and final states, which are rather insensitive to the addition of two phosphine oxide moieties in the more complex system of PPT.

Figure 5 reports the experimental P $L_{II,III}$-edge NEXAFS spectra of TPPO (upper panel) and PPT (lower panel), together with the TDDFT results obtained with the LB94 xc potential. Table 4 and Table 5 show the assignment of the experimental bands of TPPO and PPT, respectively, while the corresponding B3LYP results are reported in the Supporting Information (see Figure S4). Plots of selected KS virtual MOs are reported in Figure S6 and Figure S7 for TPPO and PPT, respectively. Also, in this case, the P 2p excitations give rise to two series of spectral features converging to the $2p_{3/2}$ and $2p_{1/2}$ ionization thresholds, which overlap due to the small SO energy splitting value (950 meV) of the $L_{II,III}$ core-hole states. The assignment is more complicated in PPT than in TPPO because of the presence, in the former, of two nonequivalent P atoms as well as of the increased density of excited states.

Again, to facilitate the spectral attribution, for both molecules the computed spectra have been deconvoluted into the two series of transitions converging to the L_{III} and L_{II}-edges.

The calculated P $L_{II,III}$-edge NEXAFS spectrum of TPPO is characterized by a lower-energy double-peaked (A−B) structure: peaks A and B are contributed by the SO partner transitions from $2p_{3/2}$ and $2p_{1/2}$ core-holes toward low-lying virtual MOs of mainly $\pi^*(C=C)$ valence antibonding character. The two peaks are separated by a SO splitting of about 0.9 eV. Their low intensity reflects the small P nd AOs weights in the π^* valence MOs and indicates therefore that P 3d AOs are not involved in the formation of the P−O bond. Peak C is contributed by the $2p_{3/2}$ transitions (subpeak b') toward final MOs with significant P diffuse s and d atomic components and some $\sigma^*(C-H)$ and $\sigma^*(P-O)$ valence antibonding characters. The L_{II} SO partner transitions (subpeak b'') contribute to peak D together with a manifold of L_{III} transitions (subpeak c') toward virtual MOs with a partial $\sigma^*(C-H)$ or $\pi^*(P-O)$ valence nature with considerable contributions of P diffuse s, d AOs. Since the SO partner of subpeak c' (subpeak c'') is centered just above the L_{III} thresholds, its analysis is not included in Table 4.

A good correspondence between the energy position of the experimental and calculated peaks is observed, apart from the lacking, in the theoretical profile, of a weak structure centered between bands B and C. The intensity distribution is also qualitatively reproduced by theory, which is, however, not able to fully account for the finer structure of bands C and D, which we tentatively associate to vibronic effects not included in the computational protocol.

Similar considerations can be made in the case of PPT. With reference to the lower panel of Figure 5, the total calculated P $L_{II,III}$-edge NEXAFS spectrum of PPT is characterized, at lower excitation energies, by a weak feature (A) which corresponds to the (P1,P2) $2p_{3/2}$ excitations toward final MOs of strong $\pi^*(C=C)$ valence antibonding character. The L_{II} SO partner transitions give rise to peak B (subpeak a''), which is also contributed by subpeak b', originating from the (P1,P2) $2p_{3/2}$ excitations toward a final π^* MO. As in TPPO, the closeness between the energy separation of a' and a'' subpeaks (about 0.9 eV) and the experimental SO splitting (0.87 eV) confirms the assignments. Subpeak b'' is located in the lower-energy region of peak C; the latter mainly derives its intensity from a manifold of transitions converging to the L_{III} threshold (subpeak c'). The implicated virtual MOs present either mixed valence/Rydberg or pure Rydberg nature. Both $\sigma^*(P-O)$ and $\sigma^*(C-H)$ components contribute to the valence character of these transitions, in line with the spectral trend found for TPPO. Subpeak c'' is located under the envelope of band D, together with L_{III} transitions to final MOs of $\sigma^*(C-H)$ or $\pi^*(P-O)$ valence antibonding character together with sizable contributions from P ns, nd AOs. In this energy region, weak transitions to diffuse orbitals are also visible. Subpeak d'' is centered at around 138 eV, just below the L_{II} threshold, and its analysis is not reported in Table 5. The main P 2p NEXAFS features are therefore conserved in going from TPPO to PPT, suggesting that the electronic behavior of the TPPO building block remains substantially unchanged when immersed in the more complex PPT.

An important point of this analysis concerns the relative energy position of the transitions toward $\sigma^*(P-O)$ and $\pi^*(P-O)$ states: the former occurs at lower energies compared to the latter (see Tables 4 and 5), while the π symmetry interaction in

the P−O bond is more stabilized compared to the σ one in the occupied MOs. These results therefore support the mechanism of negative hyperconjugation in the formation of the P−O bond[41,42] whereas the involvement of bent multiple bonds (Ω bonds[11]) to the P−O bond is ruled out.

5. CONCLUSIONS

We present a joint experimental and theoretical investigation of the electronic structure of gas-phase TPPO and PPT as obtained through XPS and NEXAFS spectroscopies at the S and P $L_{II,III}$-edge region. The experimental results have been rationalized by means of the relativistic TDDFT approach which allows the inclusion of the coupling between 1h-1p excited configurations from the 2p degenerate core holes and gives a good account of the relativistic effects (mainly spin−orbit coupling) which are necessary to describe the transitions converging to the L_{II} and L_{III}-edges.

The calculation of the S 2p and P 2p XP spectra has allowed us to analyze the BEs in terms both of the SO splitting of the 2p core-holes and of the molecular-field splitting of the $2p_{3/2}$ levels. A comparison of S 2p and P 2p XP spectra with those of the two building blocks of PPT, namely DBT and TPPO, reveals that both splittings are substantially conserved. The small increase of the S 2p experimental BEs in going from DBT to PPT is a consequence of the decreased shielding effect of the electronic charge density on sulfur due to the addition of two electron-withdrawing phosphine oxide moieties in PPT. The small decrease of the P L_{III} and L_{II} experimental BEs observed in going from TPPO to PPT can be instead rationalized by the replacement of a single phenyl ring of TPPO with one condensed ring of the DBT moiety in PPT.

The TDDFT results are accurate enough to provide a sound assignment of all absorption bands that characterize the below-threshold region of the S 2p and P 2p NEXAFS spectra. They display strong similarities to those of the PPT building blocks, DBT and TPPO, in line with the similar local environment of S and P atoms, being little affected by the increased molecular complexity of PPT. The present study complements the characterization of the electronic structure of TPPO and PPT obtained from the analysis of the C 1s and O 1s edge regions of these two molecules.[9] The intensity of the C 1s and O 1s NEXAFS spectra, which maps the C 2p and O 2p AO weights to the final MOs, derives from transitions to the low-lying delocalized π^* virtual valence orbitals, while the S 2p and P 2p NEXAFS intensities provide specific information on the higher-lying localized $\sigma^*(C-S)$ and $\sigma^*(P-O)$ virtual MOs. The results of this work indicate (i) that P 3d AOs are not involved in the formation of the P−O bond, and (ii) the energy ordering of P 2p transitions to $\sigma^*(P-O)$ and $\pi^*(P-O)$ virtual states is compatible with the traditional view of the P−O bond formation through a mechanism of negative hyperconjugation.[11] A similar study at the NEXAFS P K-edge would be useful to evaluate in detail the weight of the P 2p AO contributions to the P−O bond and will be the subject of future works.

■ ASSOCIATED CONTENT

ⓢ Supporting Information

The Supporting Information is available free of charge at https://pubs.acs.org/doi/10.1021/acs.jpcc.0c03973.

Plots of selected MOs for TPPO and PPT; B3LYP XPS and NEXAFS spectra; VWN/TZP optimized Cartesian coordinates of DBT, TPPO, and PPT (PDF)

■ AUTHOR INFORMATION

Corresponding Authors

D. Toffoli − *Department of Chemical and Pharmaceutical Sciences, University of Trieste, 34127 Trieste, Italy;* ⓞ orcid.org/0000-0002-8225-6119; Email: toffoli@units.it

A. Guarnaccio − *ISM-CNR, Institute of Structure of Matter−, Tito Scalo (PZ) and Trieste, Italy;* ⓞ orcid.org/0000-0002-7927-5845; Email: ambra.guarnaccio@pz.ism.cnr.it

Authors

E. Bernes − *Department of Chemical and Pharmaceutical Sciences, University of Trieste, 34127 Trieste, Italy*

G. Fronzoni − *Department of Chemical and Pharmaceutical Sciences, University of Trieste, 34127 Trieste, Italy;* ⓞ orcid.org/0000-0002-5722-2355

M. Stener − *Department of Chemical and Pharmaceutical Sciences, University of Trieste, 34127 Trieste, Italy;* ⓞ orcid.org/0000-0003-3700-7903

T. Zhang − *School of Information and Electronics, MIIT Key Laboratory for Low-Dimensional Quantum Structure and Devices, Beijing Institute of Technology (BIT), Beijing 100081, China; Department of Physics and Astronomy, Uppsala University, SE-751 20 Uppsala, Sweden*

C. Grazioli − *IOM-CNR, Laboratorio TASC, Sincrotrone Trieste, I-34149 Trieste, Basovizza, Italy*

F. O. L. Johansson − *Department of Physics and Astronomy, Uppsala University, SE-751 20 Uppsala, Sweden;* ⓞ orcid.org/0000-0002-6471-1093

M. Coreno − *ISM-CNR, Institute of Structure of Matter−, Tito Scalo (PZ) and Trieste, Italy*

M. de Simone − *IOM-CNR, Laboratorio TASC, Sincrotrone Trieste, I-34149 Trieste, Basovizza, Italy*

C. Puglia − *Department of Physics and Astronomy, Uppsala University, SE-751 20 Uppsala, Sweden;* ⓞ orcid.org/0000-0001-6840-1570

Complete contact information is available at:
https://pubs.acs.org/10.1021/acs.jpcc.0c03973

Notes

The authors declare no competing financial interest.

■ REFERENCES

(1) Adachi, C.; Baldo, M. A.; Thompson, M. E.; Forrest, S.R. J. Nearly 100% internal phosphorescence efficiency in an organic light-emitting device. *J. Appl. Phys.* **2001**, *90*, 5048−5051.

(2) Tang, C. W.; Van Slyke, S. A. Organic Electroluminescent Diodes. *Appl. Phys. Lett.* **1987**, *51*, 913−915.

(3) Friend, R. H.; Gymer, R. W.; Holmes, A. B.; Burroughes, J. H.; Marks, R. N.; Taliani, C.; Bradley, D. D. C.; Dos Santos, D. A.; Brédas, J.-L.; Lögdlund, M.; et al. Electroluminescence in conjugated polymers. *Nature* **1999**, *397*, 121−128.

(4) Kim, D.; Salman, S.; Coropceanu, V.; Salomon, E.; Padmaperuma, A. B.; Sapochak, L. S.; Kahn, A.; Brédas, J.-L. Phosphine Oxide Derivatives as Hosts for Blue Phosphors: A Joint Theoretical and Experimental Study of Their Electronic Structure. *Chem. Mater.* **2010**, *22*, 247−254.

(5) Tsai, Y.-S.; Hong, L.-A.; Juang, F.-S.; Chen, C.-Y. Blue and white phosphorescent organic light emitting diode performance improvement by confining electrons and holes inside double emitting layers. *J. Lumin.* **2014**, *153*, 312−316.

(6) Chapran, M.; Angioni, E.; Findlay, N. J.; Breig, B.; Cherpak, V.; Stakhira, P.; Tuttle, T.; Volyniuk, D.; Grazulevicius, J. V.; Nastishin, Y. A.; et al. An Ambipolar BODIPY Derivative for a White Exciplex OLED and Cholesteric Liquid Crystal Laser toward Multifunctional Devices. *ACS Appl. Mater. Interfaces* **2017**, *9*, 4750−4757.

(7) Sapochak, L. S.; Padmaperuma, A. B.; Vecchi, P. A.; Cai, X.; Burrows, P. E. Designing Organic Phosphine Oxide Host Materials Using Heteroaromatic Building Blocks: Inductive Effects on Electroluminescence. *Proc. SPIE* **2007**, 665506.

(8) Stöhr, J. *NEXAFS Spectroscopy*; Springer Verlag: Berlin, Heidelberg, Germany, 1992.

(9) Guarnaccio, A.; Zhang, T.; Grazioli, C.; Johansson, F.; Coreno, M.; de Simone, M.; Fronzoni, G.; Toffoli, D.; Bernes, E.; Puglia, C. PPT Isolated Molecule and Its Building Block Moieties Studied by C 1s and O 1s Gas Phase X-ray Photoelectron and Photoabsorption Spectroscopies. *J. Phys. Chem. C* **2020**, *124*, 9774−9786.

(10) Toffoli, D.; Guarnaccio, A.; Grazioli, C.; Zhang, T.; Johansson, F.; de Simone, M.; Coreno, M.; Santagata, A.; D'Auria, M.; Puglia, C.; et al. Electronic Structure Characterization of a Thiophene Benzo-Annulated Series of Common Building Blocks for Donor and Acceptor Compounds Studied by Gas Phase Photoelectron and Photoabsorption Synchrotron Spectroscopies. *J. Phys. Chem. A* **2018**, *122*, 8745−8761.

(11) Gilheany, D. G. No d Orbitals but Walsh Diagrams and Maybe Banana Bonds: Chemical Bonding in Phosphines, Phosphine Oxides, and Phosphonium Ylides. *Chem. Rev.* **1994**, *94*, 1339−1374.

(12) Blyth, R.; Delaunay, R.; Zitnik, M.; Krempasky, J.; Krempaska, R.; Slezak, J.; Prince, K. C.; Richter, R.; Vondracek, M.; Camilloni, R.; et al. The high resolution Gas Phase Photoemission beamline, Elettra. *J. Electron Spectrosc. Relat. Phenom.* **1999**, *101−103*, 959−964.

(13) Mårtensson, N.; Baltzer, P.; Brühwiler, P. A.; Forsell, J.-O.; Nilsson, A.; Stenborg, A.; Wannberg, B. A Very High Resolution Electron Spectrometer. *J. Electron Spectrosc. Relat. Phenom.* **1994**, *70*, 117−128.

(14) Pettersson, L.; Nordgren, J.; Selander, L.; Nordling, C.; Siegbahn, K.; Ågren, H. Core-Electron Binding Energies in The Soft X-Ray Range Obtained in X-Ray Emission. *J. Electron Spectrosc. Relat. Phenom.* **1982**, *27*, 29−37.

(15) True, J. E.; Thomas, T. D.; Winter, R. W.; Gard, G. L. Electronegativities from Core-Ionization Energies: Electronegativities of SF5 and CF3. *Inorg. Chem.* **2003**, *42*, 4437−4441.

(16) Eustatiu, I. G.; Francis, J. T.; Tyliszczak, T.; Turci, C. C.; Kilcoyne, A. L. D.; Hitchcock, A. P. Generalized Oscillator Strengths for Inner-Shell Excitation of SF6 Recorded with a High-Performance Electron Energy Loss Spectrometer. *Chem. Phys.* **2000**, *257*, 235−252.

(17) Haensel, R.; Keitel, G.; Schreiber, P.; Kunz, C. Optical Absorption of Solid Krypton and Xenon in the Far Ultraviolet. *Phys. Rev.* **1969**, *188*, 1375−1380.

(18) Giertz, A.; Bässler, M.; Björneholm, O.; Wang, H.; Feifel, R.; Miron, C.; Karlsson, L.; Svensson, S.; Børve, K. J.; Sæthre, L. J. High

Resolution C1s and S2p Photoelectron Spectra of Thiophene. *J. Chem. Phys.* **2002**, *117*, 7587−7592.

(19) Parr, R. G.; Yang, W. *Density Functional Theory of Atoms and Molecules*; Oxford University Press: New York, 1989.

(20) Vosko, S. H.; Wilk, L.; Nusair, M. Accurate Spin-Dependent Electron Liquid Correlation Energies for Local Spin Density Calculations: a Critical Analysis. *Can. J. Phys.* **1980**, *58*, 1200−1211.

(21) Fonseca Guerra, C.; Snijders, J. G.; teVelde, G.; Baerends, E. J. Towards an Order-N DFT Method. *Theor. Chem. Acc.* **1998**, *99*, 391−403.

(22) Baerends, E. J.; Ellis, D. E.; Ros, P. Self-Consistent Molecular Hartree-Fock-Slater Calculations I. The Computational Procedure. *Chem. Phys.* **1973**, *2*, 41−51.

(23) Bandoli, G.; Bortolozzo, G.; Clemente, D. A.; Croatto, U.; Panattoni, C. Crystal and Molecular Structure of Triphenylphosphine Oxide. *J. Chem. Soc. A* **1970**, 2778−2780.

(24) Al-Farhan, K. A. Crystal structure of triphenylphosphine oxide. *J. Crystallogr. Spectrosc. Res.* **1992**, *22*, 687−689.

(25) Diop, C. A. K.; Touré, A.; Diop, L.; Welter, R. 2-Benzoylbenzoato- kO) triphenyl (triphenylphosphineoxide-kO) tin-(IV). *Acta Crystallogr., Sect. E: Struct. Rep. Online* **2006**, *E62*, m3338−m3340.

(26) De Silva, N.; Zahariev, F.; Hay, B. P.; Gordon, M. S.; Windus, T. L. Conformations of Organophosphine Oxides. *J. Phys. Chem. A* **2015**, *119*, 8765−8773.

(27) Wang, F.; Ziegler, T.; van Lenthe, E.; van Gisbergen, S.; Baerends, E. J. The Calculation of Excitation Energies Based on The Relativistic Two-Component Zeroth-Order Regular Approximation and Time-Dependent Density-Functional with Full Use of Symmetry. *J. Chem. Phys.* **2005**, *122*, 204103.

(28) te Velde, G.; Bickelhaupt, F. M.; Baerends, E. J.; Fonseca Guerra, C.; van Gisbergen, S. J.A.; Snijders, J. G.; Ziegler, T. Chemistry with ADF. *J. Comput. Chem.* **2001**, *22*, 931−967.

(29) Stener, M.; Fronzoni, G.; de Simone, M. Time Dependent Density Functional Theory of Core Electrons Excitations. *Chem. Phys. Lett.* **2003**, *373*, 115−123.

(30) Fronzoni, G.; Stener, M.; Decleva, P.; Wang, F.; Ziegler, T.; van Lenthe, E.; Baerends, E. J. Spin-Orbit Relativistic Time Dependent Density Functional Theory Calculations for The Description of Core Electron Excitations: TiCl4 Case Study. *Chem. Phys. Lett.* **2005**, *416*, 56−63.

(31) Casida, M. E. Time-Dependent Density Functional Response Theory for Molecules. *Recent Advances in Density Functional Methods* **1995**, *1*, 155−192.

(32) Davidson, E. R. The Iterative Calculation of a Few of the Lowest Eigenvalues and Corresponding Eigenvectors of Large Real-Symmetric Matrices. *J. Comput. Phys.* **1975**, *17*, 87−94.

(33) Cederbaum, L. S.; Domcke, W.; Schirmer, J. Many-Body Theory of Core Holes. *Phys. Rev. A: At., Mol., Opt. Phys.* **1980**, *22*, 206−222.

(34) Barth, A.; Cederbaum, L. S. Many-Body Theory of Core-Valence Excitations. *Phys. Rev. A: At., Mol., Opt. Phys.* **1981**, *23*, 1038−1061.

(35) Decleva, P.; Fronzoni, G.; Lisini, A.; Stener, M. Molecular Orbital Description of Core Excitation Spectra in Transition Metal Compounds. *Chem. Phys.* **1994**, *186*, 1−16.

(36) van Lenthe, E.; Baerends, E. J. Optimized Slater-Type Basis Sets for The Elements 1−118. *J. Comput. Chem.* **2003**, *24*, 1142−1156.

(37) van Leeuwen, R.; Baerends, E. J. Exchange-Correlation Potential with Correct Asymptotic Behaviour. *Phys. Rev. A: At., Mol., Opt. Phys.* **1994**, *49*, 2421−2431.

(38) Becke, A. D. Density-functional thermochemistry. III. The role of exact exchange. *J. Chem. Phys.* **1993**, *98*, 5648−5652.

(39) Lee, C.; Yang, W.; Parr, R. G. Development of the Colle-Salvetti correlation-energy formula into a functional of the electron density. *Phys. Rev. B: Condens. Matter Mater. Phys.* **1988**, *37*, 785−789.

(40) Stephens, P. J.; Devlin, F. J.; Chabalowski, C. F.; Frisch, M. J. Ab initio calculation of vibrational absorption and circular dichroism spectra using density functional force fields. *J. Phys. Chem.* **1994**, *98*, 11623−11627.

(41) Alabugin, I. V.; Gilmore, K. M.; Peterson, P. W. Hyperconjugation. *Wiley Interdiscip. Rev.: Comput. Mol. Sci.* **2011**, *1*, 109−141.

(42) Reed, A. E.; Schleyer, P. v. R. Chemical bonding in hypervalent molecules. The dominance of ionic bonding and negative hyperconjugation over d-orbital participation. *J. Am. Chem. Soc.* **1990**, *112*, 1434−1445.